RADIO SCIENCE, VOL. 45, RS1010, doi:10.1029/2008RS003843, 2010

Fluid simulation of the collisionless plasma sheath surrounding an electric dipole antenna in the inner magnetosphere

T. W. Chevalier,[1] U. S. Inan,[1] and T. F. Bell[1]

Received 27 February 2008; revised 10 August 2009; accepted 25 August 2009; published 16 February 2010.

[1] The electrostatic sheath formation surrounding an electric dipole antenna at very low frequencies (VLF) in a magnetoplasma is examined through numerical simulation. In this paper, a hydrodynamic approach is used to solve for the nonlinear sheath dynamics of antennas located in plasmas similar to that which exists in the plasmasphere between L = 2 and L = 3 in the geomagnetic equatorial plane. The plasma environment at this location is assumed to be fully ionized and collisionless consisting of electrons and protons. Poisson's equation is used to close the system, providing the quasi-electrostatic fields within the sheath region. Sheath characteristics are given as a function of antenna drive frequency and voltage with results that are compared with existing theory. Capacitance and resistance values are given to reflect the sheath's contribution to the input impedance of the antenna. Finally, the importance of ion motion and the nonlinear sheath effects on the current, charge collection and bias voltage for the transmitting antenna are shown. The primary assumptions underlying the closure mechanisms for the infinite set of fluid moments are examined through theoretical observations and simulated comparisons of the truncation schemes. This paper constitutes one of the first works on the subject of high-voltage transmitting dipole antenna in a space plasma using a three-dimensional nonlinear formulation.

Citation: Chevalier, T. W., U. S. Inan, and T. F. Bell (2010), Fluid simulation of the collisionless plasma sheath surrounding an electric dipole antenna in the inner magnetosphere, *Radio Sci.*, *45*, RS1010, doi:10.1029/2008RS003843.

1. Introduction

[2] The study of electromagnetic wave propagation and wave-particle interactions in the Earth's radiation belts has received a great deal of interest [*Carpenter and Anderson*, 1992; *Carpenter et al.*, 2003; *Bell et al.*, 2004; *Platino et al.*, 2005]. Along with electromagnetic waves launched from ground based VLF transmitters, naturally occurring VLF radiation such as whistlers injected by lightning discharges and hiss and chorus emissions generated by the energetic magnetospheric plasma have been shown to influence the populations of these highly energetic electrons that reside within the Earth's radiation belts [*Abel and Thorne*, 1998]. It has been recently proposed [*Inan et al.*, 2003], that space-based transmitters may be used as in situ wave-injection instruments for the purpose of mitigating unwanted and harmful enhancements of energetic electron fluxes in the inner radiation belt. As suggested by *Albert* [2001], the dominant mechanism behind the precipitation of these energetic particles is pitch angle diffusion in the course of cyclotron resonant wave-particle interactions by whistler mode waves.

[3] Whether operating as transmitting or receiving elements, electric dipole antennas in a magnetoplasma are surrounded by an electrostatic sheath. This sheath can significantly alter the antenna properties (both near and far field) relative to those which would be in effect if the plasma remained uniform near the antenna surface. For receiving purposes, the sheath is on the order of a few Debye lengths and is well approximated by existing analytical theory. However, when used for transmit applications requiring the driving of the transmitting element at large voltages far in excess of the surrounding plasma potential, the sheath is highly nonlinear and its structure is generally not well known.

[4] Since the pioneering work of *Langmuir* [1929] and later by *Bohm* [1949] which formed the basis of the

[1]Department of Electrical Engineering, Stanford University, Stanford, California, USA.

0048-6604/10/2008RS003843$11.00

sheath models found in most literature on the subject, there has been considerable work performed in the areas of theory, simulation and experiment, some of which is now discussed.

1.1. Sheaths and Electric Dipole Antennas

[5] Early attempts at modeling the sheath effects on the terminal properties of dipole antennas include *Mlodnosky and Garriott* [1963] who used small signal analysis coupled with a fixed-capacitor analogy to derive closed-form expressions for the sheath radius, capacitance and resistance of a VLF dipole antenna moving through an ionospheric plasma. *Shkarofsky* [1972] extended the analysis of *Mlodnosky and Garriott* [1963] to include large signal excitation and the effects of an induced electromotive force (emf) resulting from the drift motion of the antenna at orbit speed (i.e., due to $\mathbf{v} \times \mathbf{B}_0$). The following year *Baker et al.* [1973], using the same linear theory, incorporated a DC bias into their model resulting from spacecraft charging between the antenna and the satellite body on which the antenna was mounted. *Mlodnosky and Garriott* [1963], *Shkarofsky* [1972], and *Baker et al.* [1973] all used very crude first order approximations of the current and voltage on the antenna and greatly simplified the description of the sheath region through approximations such as uniform charge density and a simple exponential voltage dependence through the sheath. More recently, *Song et al.* [2007] used a theoretical formulation based upon that of *Shkarofsky* [1972] to analytically determine the terminal properties and sheath characteristics surrounding electrically short dipole antennas in the inner magnetosphere at large drive voltages relative to the ambient plasma potential. However, *Song et al.* [2007] ignored the ion current to the antenna, which is crucially important as we show later in the paper.

[6] In general, analytical sheath models are only valid under the assumption that $q\Phi/k_BT \ll 1$ where q is the charge of the particle, Φ is the potential, T is the temperature and k_B is Boltzmann's constant. This assumption allows for an implicit linearization of the set of fluid equations providing the steady state equilibrium distribution of the electrons within the sheath modified by the Boltzmann factor: $n_e = n_0 \exp(-q_e\Phi/k_BT)$, where n_e is the density variation of the electrons, n_0 is the ambient density of the quasi-neutral bulk plasma, and the quantity $\exp(-q_e\Phi/k_BT)$ is the Boltzmann factor for electrons.

1.2. Numerical Simulation Work

[7] When nonlinear behavior is prevalent and the simplifying assumptions underlying an analytical treatment are no longer justified, numerical simulation provides an invaluable tool for determination of antenna behavior in a plasma. Numerical methods generally fall into the categories of kinetic and fluid approaches.

[8] Particle In Cell (PIC) codes are used when wave-particle interactions are of interest since a fluid code by its nature cannot, in general, properly describe the influence of single particles. In a fluid approach, this individual particle motion is averaged out into collective behavior. A number of authors have examined the sheath dynamics and related phenomena using a PIC approach.

[9] Time-dependent sheath dynamics resulting from both positive and negative step function voltage changes on an electrode in a collisionless nonmagnetized plasma were also studied for both cylindrically and spherically symmetric geometries [*Calder and Laframboise*, 1990; *Calder et al.*, 1993]. The magnitude of the drive potentials used by *Calder and Laframboise* [1990] and *Calder et al.* [1993] were on the order of 10^3 times the background plasma potential. Langmuir oscillations amplified by the electron-ion two-stream instability were evident in these simulations, which as noted by *Calder and Laframboise* [1990] can also be treated with a fluid description. However it was also suggested by *Calder and Laframboise* [1990] that plasma ringing exists due to the abrupt voltage changes which can affect the transient current collection on the electrodes for many plasma periods that cannot be accounted for in a fluid treatment. A similar analysis was made by *Borovsky* [1988] using a PIC approach in which he varied the potential on the electrode and noted the plasma ringing effects which were also amplified by the electron-ion two-stream instability.

[10] Despite their potential deficiencies, fluid models have successfully been applied to the sheath problem with good comparisons with PIC techniques. Some of the most pertinent works were in relation to the recent Space Power Experiments Aboard Rockets (SPEAR) program. This work includes *Ma and Schunk* [1989, 1992a, 1992b] and *Thiemann et al.* [1992], who used a two-moment fluid analysis to study the temporal evolution of particle fluxes on high-voltage spheres in a collisionless nonmagnetized plasma noting abrupt changes to the current collection as a result of the initial sheath formation. For large negative voltages, *Ma and Schunk* [1992a] and *Thiemann et al.* [1992] were able to reproduce the transient plasma ringing found in earlier PIC codes such as *Borovsky* [1988], *Calder and Laframboise* [1990], and *Thiemann et al.* [1992] (who performed a PIC-fluid comparison). *Labrunie et al.* [2004] performed a comparison between a one-dimensional Vlasov-Poisson kinetic simulation and a three-moment fluid code by studying ion-acoustic waves in a collisionless plasma. These authors highlight that fluid codes, even in the collisionless limit, can be very accurate, provided that certain conditions are met. The most relevant of these conditions is that the characteristic

speeds of the phenomena of interest are not on the same order as the particle thermal velocities in which Landau damping is of concern.

[11] In this paper, we have developed an electrostatic simulation tool to examine the dynamics of the collisionless sheath using a two-species plasma fluid formulation. The antennas of interest here are located at magnetospheric points corresponding to $L = 2$ and $L = 3$ where the plasma consists of a fully ionized electron-proton plasma. Our paper utilizes a Finite-Volume (FV) method with the electrostatic fields provided through solution of Poisson's equation. Whereas past work has primarily involved the study of antennas using linear analysis, or in the case of the sheath formation has considered only DC potentials applied to two-dimensional symmetric geometries, we extend this past analysis to include AC applied potentials and three-dimensional geometries using fully nonlinear formulations. This paper thus presents significant contributions in the area of antenna-plasma coupling, most notably on the subject of sheath dynamics surrounding electric dipole antennas.

2. Fluid Formulation

[12] Our fluid formulation uses a macroscopic multifluid approach to solve for the nonlinear sheath dynamics. The fluid model is comprised of moments of the Vlasov equation $\mathcal{F}_v$ for each particle species given by equation (1):

$$\mathcal{F}_v(\mathbf{v}, \mathbf{r}, t) = \frac{\partial f}{\partial t} + (\mathbf{v} \cdot \nabla_{\mathbf{r}})\mathsf{f} + \left[\frac{\mathbf{F}}{m} \cdot \nabla_{\mathbf{v}}\right]\mathsf{f} = 0 \qquad (1)$$

where m is the mass, and $\mathbf{F} = q(\mathbf{E} + \mathbf{v} \times \mathbf{B})$ is the Lorentz force with charge q, velocity vector $\mathbf{v}$, electric field $\mathbf{E}$ and magnetic field $\mathbf{B}$. Since the bulk of the plasma between $L = 2$ and $L = 3$ is virtually cold ($\sim$2000°K) consisting of very low energy particles [*Bezrukikh et al.*, 2003], we assume that our initial distribution for each species is a Maxwellian distribution as in the works of *Calder and Laframboise* [1990] and *Calder et al.* [1993].

2.1. Moments of the Vlasov Equation

[13] The series of moments that comprise each species of our two fluid model are derived by multiplying each term in the Vlasov equation by powers of $\mathbf{v}$ and then integrating the resultant equation over all velocity space. The fluid transport model comprising the first four moments given by equations (2a)–(2d) (which are found in the work of *Chust and Belmont* [2006]) correspond to density, momentum, pressure, and heat flux, respectively:

$$\partial_t(nm) + \nabla \cdot (nm\mathbf{u}) = 0 \qquad (2a)$$

$$\partial_t(nm\mathbf{u}) + \nabla \cdot (nm\mathbf{u}\mathbf{u} + \mathbf{P}) + S_{\mathrm{M}} = 0 \qquad (2b)$$

$$\partial_t(\mathbf{P}) + \nabla \cdot (\mathbf{u}\mathbf{P} + \mathbf{Q}) + S_{\mathrm{P}}{}^{\mathrm{sym}} = 0 \qquad (2c)$$

$$\partial_t(\mathbf{Q}) + \nabla \cdot (\mathbf{v}\mathbf{Q} + \mathbf{R}) + S_{\mathrm{Q}}{}^{\mathrm{sym}} = 0 \qquad (2d)$$

$$S_{\mathrm{M}} = -nq(\mathbf{E} + \mathbf{u} \times \mathbf{B})$$

$$S_{\mathrm{P}} = \{\mathbf{P} \cdot \nabla(\mathbf{u}) + \mathbf{\Omega}_{\mathbf{c}} \times \mathbf{P}\}$$

$$S_{\mathrm{Q}} = \left\{\mathbf{Q} \cdot \nabla(\mathbf{u}) + \mathbf{\Omega}_{\mathbf{c}} \times \mathbf{Q} - \mathbf{P}\nabla \cdot (\mathbf{P})\frac{1}{nm}\right\}$$

[14] In equations (2c) and (2d), $\mathbf{\Omega_c}$ and $\mathbf{R}$ represent the gyrofrequency vector along the magnetic field and the fourth order moment respectively, while the superscript 'sym' denotes a symmetric tensor.

[15] In this paper, we develop three warm plasma models based upon subsets of equations (2a)–(2d) using various closure relations that are discussed in section 3. We then compare results of the various truncation relations through simulation for both magnetized and unmagnetized plasmas in the context of sheath formation. This comparison allows us to verify the applicability of our simulation tool since the regions of validity of the fluid approach as applied to sheath formation are not readily apparent, as outlined by *Chust and Belmont* [2006].

2.2. Instabilities and Resonances

[16] Though the fluid model can provide a very accurate description of plasma behavior over a wide range of conditions, there are some phenomena for which a fluid description may be inadequate. These phenomena are usually associated with wave-particle interactions, since the behavior of individual particles is not taken into account as they would be, for example, in PIC method. The potential importance of such effects in our fluid-based sheath simulations is discussed below.

2.2.1. Two-Stream Instability and Landau Damping

[17] In the simulations of *Borovsky* [1988], *Calder and Laframboise* [1990], *Ma and Schunk* [1992a], *Thiemann et al.* [1992] and *Calder et al.* [1993], it was seen that transient electron plasma oscillations formed during the initial step response of the system to the high voltage excitation on spherical electrodes, when using both PIC and fluid approaches. *Calder and Laframboise* [1990] additionally noted that these same large plasma ringing effects were driven to large amplitude by the ion-electron two-stream instability in the absence of an external magnetic field which they stated that a fluid code can capture. *Calder et al.* [1993] observed that this instability was present only in simulations of positively stepped

electrodes, since for negatively stepped potentials, the electrons were completely evacuated from the sheath region due to their much higher mobility. The ions left inside the sheath had no electrons with which to interact and thus the instability could not develop. For the case of a positive applied potential, the ions are not fully depleted from the sheath region since they are much heavier.

[18] The same PIC simulations suggested that Landau damping was also negligible since the phase velocity of Langmuir modes is much larger than particle thermal velocity [*Calder and Laframboise*, 1990]. Later, *Thiemann et al.* [1992] determined that not only could a two-moment fluid code reproduce the oscillation in general character, but that some of the oscillations present in the PIC code were due in large part to numerical noise resulting from undersampling the particle distribution function, an inherent problem in large-scale PIC codes.

[19] The remaining question is whether or not the electron-electron two stream instability is present during sheath formation since a fluid code cannot capture this instability. An electron-electron two-stream instability has not been observed in any PIC plasma sheath simulations that we are aware of, including those referenced herein. This result is perhaps due to the symmetry of the cases considered. Directly counter-streaming electrons would only interact from opposing sides of the sheath, in which case they would hit the conductor and be absorbed. Any electrons that do not collide with the antenna surface would have their trajectories randomized, most notably in the case of an ambient magnetic field, and would therefore not satisfy the condition for a two-stream electron-electron instability.

2.2.2. Particle Trapping and Secondary Emission

[20] The effect of particle trapping in the sheath region surrounding high voltage conductors has been previously studied [*Parker and Murphy*, 1967; *Palmadesso*, 1989]. *Parker and Murphy* [1967] used theoretical arguments involving conservation of energy and angular momentum to derive a closed form solution for the radius in which electron trapping would occur for DC applied potentials surrounding spherical electrodes in a magnetic field. However, in the PIC simulations of *Calder et al.* [1993] involving large DC applied potentials applied to electrodes, it was shown that only the positive ions are trapped as a result of biasing the electrode rapidly. The electrons would not be trapped since they would have comparable orbits with the ions in the steady state fields when their energies are equivalent, despite the large ion-electron mass ratio. Therefore, since we consider cases in which the potential on the antenna is slowly varying at VLF frequencies, we would not expect particle trapping to be of concern.

[21] Secondary emission of electrons occurs when a conductor is biased to a high voltage for which electrons or ions accelerated to high energies impact the surface of the conductor, and kick off secondary electrons. For the case of a thin wire antenna in three dimensions, the secondary emission effect would be much less pronounced since the actual surface area over which secondary electrons sputter from the antenna elements is very small compared to the conductor surface area in the one-dimensional PIC simulations of *Franklin and Han* [1988]. In addition, the radial symmetry of the antenna geometry provides further evidence against the formation of a beam which would excite the instability.

3. Electrostatic Model

[22] The warm plasma formulation incorporates all nonlinear effects for each fluid moment utilized, coupled with Poisson's equation for the quasi-electrostatic fields. The details of this approach along with the closure approximations and simulation techniques used are discussed below.

3.1. Closure Approximations

[23] In the warm plasma fluid approximation, no assumptions of linearity are made and thus all convective terms in the system of moments defined by equations (2a)–(2d) are preserved. Three warm plasma closure mechanisms are considered in this paper. The first closure relation is the isothermal approximation which assumes that the pressure tensor $\mathbf{P}$ is diagonal with each element p given by the ideal gas law relation $p = nk_BT$, where T is the plasma temperature in all directions. In this isothermal approximation, the system of equations representing the plasma is given by the first two fluid moments shown in equations (2a)–(2b).

[24] The second closure relation assumes that the system is adiabatic (i.e., $\nabla \cdot \mathbf{Q} = 0$) and thus all terms involving the heat flux tensor are zero. In this adiabatic formulation, the plasma is represented by the first three moments of equation (1) given as equations (2a)–(2c).

[25] The third closure relation makes no assumptions on adiabaticity and includes the heat-flux tensor as well as an approximation on the fourth order moment $\mathbf{R}$. The system of equations using this nonadiabatic closure approximation is given by equations (2a)–(2d). In this case, our closure relation is based on an assumption concerning the next highest moment $\mathbf{R}$ in equation (2d). We follow the example of *Chust and Belmont* [2006] in this case, and assume that each element of the tensor $\mathbf{R}$ is given by $r_{\alpha\beta\gamma\kappa}$ and satisfies the relation $r_{\alpha\beta\gamma\kappa} = p_{\alpha\beta}p_{\gamma\kappa}/(nm)$, where p are elements of the pressure tensor, n is the local number density, m is mass and α, β, γ and κ are indices which span the dimensions $\hat{x}$, $\hat{y}$, and $\hat{z}$. This assumption, as with all other closure relations given, is equivalent to assuming that the distribution function remains sufficiently compact

and relatively symmetric about the mean (thermal velocity) so that the first few moments provide an adequate description of the distribution.

3.2. Quasi-Electrostatic Approximation

[26] Though early antenna work involving sheath formation makes unjustified simplifying assumptions [*Mlodnosky and Garriott*, 1963], some insight into the relative size of the sheath can be gained so as to gauge whether or not a quasi-electrostatic solution is justified at high voltages. The work of *Laframboise* [1997] provides modifications to the Boltzmann factor based on various criteria for spacecraft charging. Using *Laframboise* [1997] as a reference coupled with the sheath radius approximations of *Mlodnosky and Garriott* [1963], we can deduce that even at 1000 V applied potential on the antenna, the sheath radius would only be a couple of meters at VLF frequencies, still much smaller than the smallest electromagnetic wavelength. A first order approximation of the wave electric field in Maxwell's equations at 1000 V does not produce a wave magnetic field that has a magnitude on the same scale as the background magnetic field. Likewise, a comparison of the displacement and conduction current terms at VLF frequencies yields the relation $\sigma \gg \omega\epsilon_0$ when $\omega_p \gg \omega$, providing further justification for the electrostatic approximation since it is the conduction current term that is dominant. Therefore, a quasi-static approach is justified and Poisson's equation can be used to close the system of fluid equations given by:

$$\nabla^2\Phi = \frac{-\sum_\alpha \rho_\alpha}{\epsilon_0} \tag{3a}$$

$$\vec{E} = -\nabla\Phi \tag{3b}$$

where Φ is the potential, $\vec{E}$ is the electric field, ϵ_0 is the permittivity of free space, and the charge density ρ is summed across all species α, with $\alpha = 2$ representing only electrons and protons in our model. The use of Poisson's equation removes the electromagnetic time-stepping constraint and enforces a triangular current distribution along the length of the antenna.

3.3. Simulation Development

3.3.1. Finite Volume Method

[27] The warm plasma model uses a finite-volume method to solve for the fluid dynamics and an iterative matrix solver for the solution of Poisson's equation which provides the electrostatic fields. The simulation tool uses the PETSc framework [*Balay et al.*, 2004].

[28] The FV method we have chosen utilizes the central differencing formulation of *Kurganov and Tadmor* [2000]. This method is second order accurate in space and is coupled with the strong stability preserving (SSP) Explicit Runge-Kutta (ERK) time-integration schemes of *Spiteri and Ruuth* [2002] which are up to fourth order accurate in time. A variable time step algorithm is employed in our simulation tool since the fluid velocities are constantly changing in time due to the dynamic structure of the sheath. This adaptive time step is most critical during the early stages involving transient sheath formation.

3.3.2. Multiscale Simulations

[29] Multiscale plasma simulation regions which have been used by previous authors [*Parker et al.*, 1993a, 1993b; *Wang and Wendt*, 1999] are very useful in minimizing the computational requirements by utilizing spatial scales that are appropriate to the region of interest. In the context of sheath dynamics, one typically uses cell sizes on the order of a Debye length λ_D within the sheath region, in order to capture the shielding effects without spatial aliasing. Outside of the sheath region however, the scale lengths are generally larger in order to capture physics such as Langmuir oscillations and electromagnetic waves.

[30] An adjusted mass ratio is often used in simulations [*Calder and Laframboise*, 1990; *Calder et al.*, 1993] to reduce the computational requirements as long as the underlying principal physics is not significantly modified i.e., $m_i \gg m_e$. In our simulations, we assume a proton-electron temperature ratio of $(T_p/T_e) = 1.0$ and in some of the simulation results presented in section 4, a mass ratio of $(m_p/m_e) = 200$. In addition, we have verified through simulation that application of the correct mass ratio of $(m_p/m_e) = 1836$ provides qualitatively similar behavior to using the scaled mass ratio of $(m_p/m_e) = 200$ for the results presented in section 4. Use of the scaled mass ratio significantly alleviates some of the computational burden as discussed. These assumptions are clearly marked in the corresponding results section.

3.3.3. Boundary Conditions

[31] Boundary conditions are implemented for both Poisson's equation and the plasma fluid equations. In either case, these relations must be specified on the plasma-facing surface of the material immersed within the plasma (e.g., the antenna surface) as well as at the exterior of the simulation domain. The boundary conditions used in our warm plasma model for the fields and the fluid are now discussed.

[32] On the surface of the conductor there are two distinct types of boundary conditions implemented for the solution of Poisson's equation, based on whether or not the conducting element is active or passive. If the element is active, as in the case of a transmitting antenna, the potential on the conducting surface is forced to be the driving potential. If the element is passive, the situation is slightly more complex. A conducting body immersed in a plasma collects space charge, creating a floating DC

potential on the conducting surface as a result of the different mobility of each plasma species. At a temperature of T = 2000°K, this negative DC floating potential has a magnitude on the order of a few tenths of an electron volt (eV). The passive condition corresponds to the initial conditions of the fluid simulation since it is the initial state of any nontransmitting element in a plasma. Therefore, in our simulations, this initial floating state of the conductor is first run as a separate self-consistent simulation, providing the initial conditions used in the active antenna simulations. The solution of Poisson's equation for the floating conductor utilizes the capacity matrix method developed by *Hockney and Eastwood* [1981].

[33] At the edge of the computational space we assume the plasma to be quasi-neutral far from the sheath region and therefore implement a Dirichlet boundary condition with the potential at the outer boundary of the domain equal to zero.

[34] The boundary conditions at the conductor surface for each of the fluid moments are found by integrating an assumed Maxwellian distribution in either the left or right half plane for each quantity that is crossing an imaginary flux surface in a single direction. For the first two moments, the distribution function is assumed to be a drifting Maxwellian distribution. For the pressure and heat flux moments which only take into account the thermal motions of the particles, the distribution function is modeled as a nondrifting Maxwellian.

[35] For instance, the unidirectional velocity v_s of a fluid element normal to the surface of a conductor located in the right half plane is given by equation (4):

$$v_s = \frac{1}{2} e^{-v_0^2/\left(2v_{th}^2\right)} \sqrt{\frac{2}{\pi}} v_{th} + \frac{1}{2}\left[1 + erf\left(\frac{v_0}{\sqrt{2}v_{th}}\right)\right] v_0 \quad (4)$$

where v_0 is the Maxwellian drift velocity, v_{th} is the thermal velocity, and *erf*[ ] represents the error function. At the outer most boundary of the simulation domain, Neumann conditions are used for fluid moments. The velocity term of equation (4) is used at the surface of the antenna when solving the system of moments in equations (2a)–(2d). This boundary condition which is based strictly on the distribution function adjacent to the conductor surface is an analytical boundary condition that is a more complete form of analogous BC's used in other hydrodynamic codes such as drift diffusion models. In these formulations, the common assumption is that the average drift velocity is zero. When the plasma constituents hit the antenna surface, they are absorbed and in the case of the antenna without a mechanism that removes excess charge, the whole system is negatively biased as shown in section 4.3.3. Inside of the antenna structure, there is no concept of a fluid element and this goes for any simulation of this type as these fluid quantities are meaningless. Other than the charge collection reverse biasing the antenna and the fact that we are not considering the entire spacecraft body in this effort, the plasma that hits the antenna is assumed to be completely lost and is no longer part of the simulation.

4. Results

[36] We begin by validating our fluid model in the context of one-dimensional planar sheath simulations through comparison with the analytical work of *Bohm* [1949]. These analytical formulas provide a reasonable approximation to the floating sheath and are documented in many plasma physics textbooks [*Bittencourt*, 2003, pp. 279–288]. Next, we examine the effect of various closure mechanisms on the formation of the sheath around a two-dimensional infinite line source considering an isotropic plasma. Finally, simulation results for the sheath surrounding a 20 m long electric dipole antenna in three dimensions are presented for three case studies. Geometric and terminal impedance characteristics of the dipole antenna are highlighted in interpreting the results of these simulation runs.

4.1. One-Dimensional Planar Sheath

[37] To test our warm plasma simulation tool, we consider a collisionless, fully ionized plasma with parameters corresponding to L = 2 in the equatorial plane being f_{pe} = 401 kHz and f_{ce} = 110 kHz for the plasma and gyrofrequencies respectively. The Debye length for this plasma is $\lambda_D \simeq 7$ cm and the proton-electron mass ratio is $(m_p/m_e) = 1836$. The cell size in the simulation domain is chosen as to capture any Debye-scale effects under these low-voltage conditions and is made to be Δx = 2.5 cm, with the entire space being 2.5 m in length or roughly 36 λ_D. For these one-dimensional planar sheath calculations we neglect the magnetic field. A floating (no applied potential) conducting wall is placed in the left half plane of the 1-D simulation space with the initial number densities of electrons and protons made constant across the simulation domain. In addition, the initial velocities of both the protons and electrons are zero with the only nonzero element being the directed drift-velocity boundary condition specified in equation (4). The boundary condition of equation (4) is the initial condition that allows for the electrons to initially collect on the surface of the conductor and eventually form a negative potential barrier.

[38] Figure 1 represents a comparison between our fully nonlinear warm plasma model and the analytical results of *Bohm* [1949]. Simulations were performed using all three warm plasma closure mechanisms outlined in section 2. However, there were negligible differences between the simulation runs for the one-dimensional

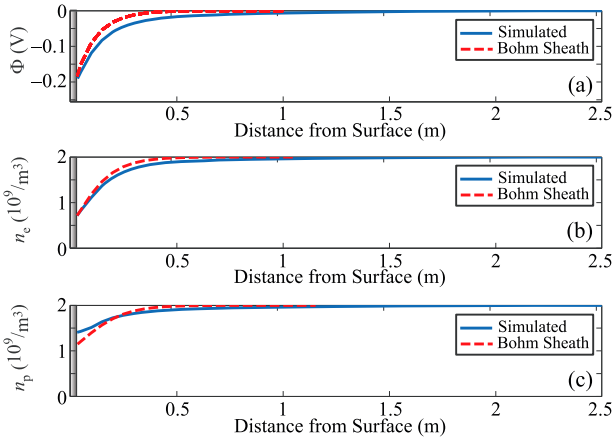

Figure 1. Comparison of 1-D planar sheath simulation with analytical results of Bohm. (a) Potential. (b) Electron number density. (c) Proton number density.

floating sheath since we are in an essentially linear regime. Thus, only the simulation results obtained by using the full nonadiabatic closure assumption represented by equations (2a)–(2d) are shown.

[39] Figure 1 presents comparisons of our sheath model with that of *Bohm* [1949] for the potential, electron density and proton density variations. It can be seen from Figure 1 that our warm plasma results are in very good agreement with the analytical results, as to be expected for the case of a floating potential. The floating potential on the conducting surface as shown in Figure 1a is wall $\Phi_{wall} \simeq -0.2$ V, which is slightly less than the background plasma potential.

[40] Unlike the analytical results of *Bohm* [1949] which force a steady state sheath condition, our simulations let this condition develop naturally in a self consistent manner. The total simulation time to reach the quasi-steady state condition represented by our model in Figure 1 was about $t = 5$ ms which corresponds to 2000 τ_{pe}, where τ_{pe} is an electron plasma period equal to 2.5 μs at $L = 2$. If the 5 ms simulation time was to represent the period of an AC voltage source, the steady state sheath would develop on scales corresponding to the period of a 200 Hz sine wave, a frequency far lower than the VLF range for the wave-particle interaction applications that motivate our study. In addition, with a plasma potential of ~0.2 eV at $L = 2$, application of even 1 V across the antenna elements would already imply a regime in which the linear analytical theory is not valid. For the collisionless plasma considered here, it is thus evident, based on the timescales involved in sheath formation, that the distribution function never reaches the steady state equilibrium described by the Boltzmann factor for a source that is varying at VLF frequencies. Therefore, analytical sheath derivations that utilize this Boltzmann factor for voltages in excess of the plasma potential for anything other than DC applied potentials in a collisionless plasma are questionable. On the other hand, collisions such as those present in a dense ionospheric plasma, could certainly aid in speeding up the relaxation of the distribution function back to a Maxwellian state over time scales comparable to or less than the period corresponding to VLF frequencies [*Mlodnosky and Garriott*, 1963; *Baker et al.*, 1973].

[41] Virtually all of the sheath derivations surrounding dipole antennas in the past analytical work mentioned in section 1.1 relied on the Boltzmann factor either explicitly or implicitly in their formulation. This follows from the fact that these works, in general, used a linearized plasma analysis and by definition cannot account for sheath formation self-consistently. The potential energy must be less than the thermal energy in deriving the Boltzmann sheath model as mentioned in the original works of *Langmuir* [1929] and *Bohm* [1949]. Since these aforementioned dipole antenna papers use linearized plasma analysis, their results are only valid for applied potentials corresponding to energies much less than the thermal energy as this is the only regime for which linearized plasma analysis is valid and for which the Boltzmann factor can be analytically derived. Otherwise, the first two linearized moments (continuity and momentum) cannot accurately capture the deviation from the equilibrium distribution function. Additionally, cold plasma analysis (linear) must make the assumption that the potential energy is much smaller than the thermal energy with this linearization being applicable only to small applied potentials as seen on receiving antennas. Large applied fields would significantly perturb the background number densities far beyond the small perturbations assumed by a linear analysis. The Boltzmann factor essentially provides a theoretical limit beyond which one must use nonlinear warm or hot plasma analysis.

[42] Without the finite thermal effects inherent in the warm plasma treatment, one would not develop any sheath self consistently, let along a high voltage sheath, since it is precisely the difference in electron and ion mobilities corresponding to their relative thermal motions that produces the initial floating sheath. The electron and ion densities surrounding a floating conductor (nontransmitting) in a plasma can vary as much as 50% of the background density which represent a significant deviation from the ambient densities present. Since a linearized cold plasma methodology assumes negligible deviation from the ambient values, this approach is not valid even for obtaining a zero-applied voltage sheath.

4.2. Two-Dimensional Infinite Line Source

[43] The purpose of the two-dimensional studies is twofold. The first is to determine the importance of the

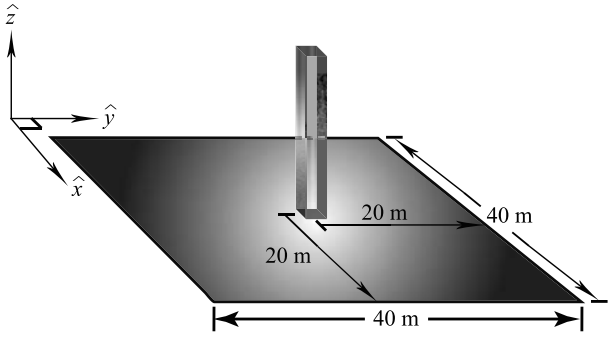

Figure 2. Conceptual drawing of two-dimensional simulation region.

proton dynamics in sheath formation. The second is to compare the various truncation schemes in order to gauge the importance of higher order moments in the fluid formulation for characterizing the time-varying sheath. In the interest of limiting the computational demands imposed by keeping the full heat-flux tensor in higher dimensions, we consider only the isothermal and adiabatic approximations for all subsequent 2-D simulation runs.

[44] Using our validated fluid model, we examine the sheath structure surrounding a two-dimensional infinite line element. This study considers a two-dimensional infinite line source in an isotropic plasma with parameters corresponding to $L = 3$ where the ambient background number densities of the plasma are assumed to be 10^9 m^{-3} for both species. We use an artificial proton-electron mass ratio of $(m_p/m_e) = 200$; a commonly used practice in order to ease the computation burden [*Calder et al.*, 1993]. The scaled proton plasma frequency in this case is $f_p = 20$ kHz. The simulation uses Neumann boundary conditions for the fluid at the edge of the space and any particles hitting the line source are completely absorbed as in the planar sheath simulation of the previous section. A sketch of the simulation domain is shown in Figure 2.

[45] We examine the time-varying sheath formation using a quasi-electrostatic approach as discussed earlier. This approach involves the use of Poisson's equation in which a sinusoidal potential is applied to the line element with a source frequency of $f_s = 25$ kHz and peak potential of approximately 1000 times the background plasma potential, which is ~172 V.

4.2.1. Proton Dynamics

[46] In order to determine the importance of the proton dynamics in sheath formation, we consider RF frequencies both above and below the proton plasma frequency. To illustrate the density variations within the sheath, we assume an isotropic plasma and recognizing the resulting azimuthal symmetry, we take a vertical $\hat{y}\hat{z}$ slice plane through the line element and plot the resulting potential and density profiles using a 1-D representation. Furthermore, we use the full adiabatic (three moment) approximation for this purpose.

[47] At time $t = 0$ s, the sinusoidal potential starts with the positive cycle. During the initial transient response, the protons are pushed away from the line source while the electrons accelerate toward the antenna and are collected. Due to their inertia, and the fact that the source frequency is in the vicinity of the proton plasma frequency, the majority of the protons traveling outward from the conductor cannot quickly respond to the change in electric field as the potential switches to the negative portion of the cycle and are permanently displaced from the sheath region. This displacement forms an evacuated or proton-depleted region for which the only substantial current collection on the line element is now due predominantly to the electron response. Figure 3 depicts the potential and density profiles at two specific times during this initial transient response corresponding to the maximum and minimum potentials during the first cycle of the sinusoidal waveform represented by t^+ and t^- respectively.

[48] During the negative potential cycle denoted by t^- in Figure 3, the electrons are pushed away from the sheath region, but due to their higher mobility, surpass the outward propagating proton wavefront. Since the tendency of the plasma is to neutralize any electric field perturbations that may exist, the electrons which exhibited the initial overshoot relative to the outward propagating protons start to electrostatically shield the proton density perturbation, forming plasma frequency oscillations at the sheath edge. After several sinusoidal cycles, this

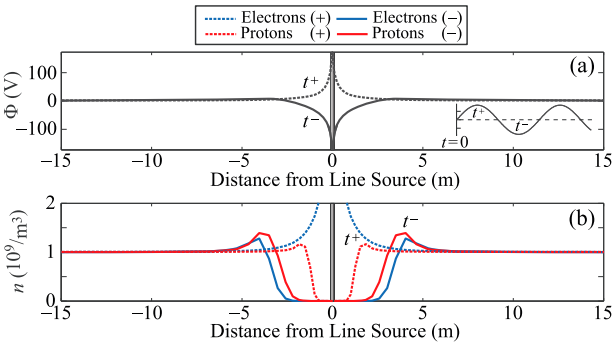

Figure 3. Transient response of 2-D simulation at $L = 3$. The symbols t^+ and t^- correspond to the first positive and negative peaks of the potential cycle for the 25 kHz sinusoidal source. All quantities shown by a dashed line correspond to t^+, and all solid lines correspond to quantities at t^-. (a) Potential variation. (b) Electron and proton number densities.

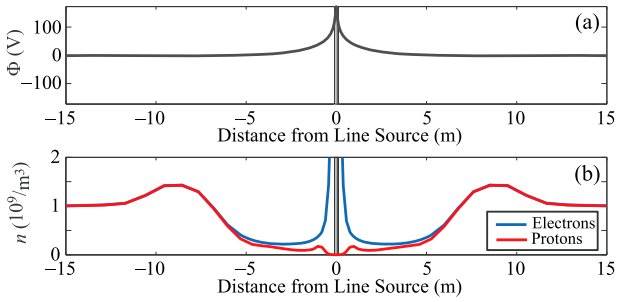

Figure 4. Snapshot during positive potential cycle of infinite line source. (a) Potential. (b) Electron and proton number densities.

double layer ceases to exist, forming an outward propagating ion acoustic wave, which is shielded by the electrons and eventually leaves the space. This behavior is not seen in the analytical formulation of *Song et al.* [2007] for which the proton motion was neglected since it was thought that the much heavier mass of the protons would essentially make them immobile.

[49] The steady state situation near the line element is represented by Figures 4 and 5 which display time snapshots of the potential and density profiles for the electrons and protons of our two species plasma after a number of periods of the 25 kHz applied potential (which is 5 kHz above the proton plasma frequency) by which time the response is periodic (except for the outward propagating density disturbance).

[50] During the positive cycle, the few ions that are left in the sheath region are repelled from the line element, whereas the electrons instantaneously react to the sinusoidal varying potential since the operating frequency is well below the electron plasma frequency which is roughly f_{pe} = 284 kHz at L = 3.

[51] At a much later time, the density disturbance exits the simulation domain and the electron and proton density profiles remain relatively unchanged at a distance

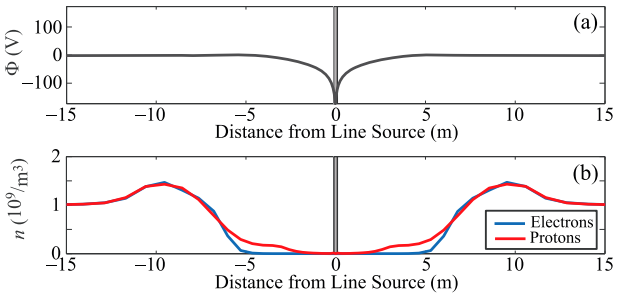

Figure 5. Snapshot during negative potential cycle of infinite line source. (a) Potential. (b) Electron and proton number densities.

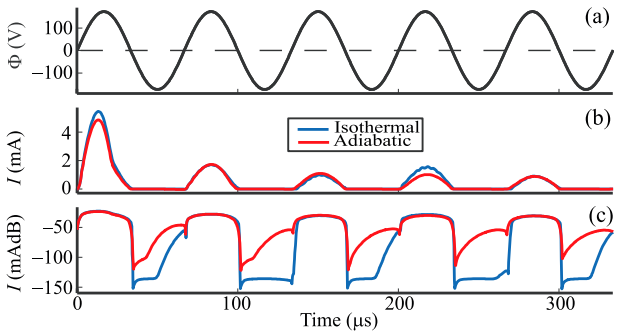

Figure 6. Current-voltage relationship for isotropic plasma with sinusoidal applied potential at 15 kHz. Blue, two moments; red, three moments. (a) Potential. (b) Current. (c) Current in dB.

of up to 7 m from the conductor. Beyond this point, the number density of both species is approximately equal to the ambient density of the plasma.

4.2.2. Comparison of Isothermal and Adiabatic Closure Conditions for Sinusoidal Excitation

[52] In this section, we compare the isothermal and adiabatic closure relations for an AC driven line element operating in an isotropic plasma by comparing the current-voltage characteristics on the infinite line element. We consider two frequencies that are respectively 5 kHz above and below the proton gyrofrequency.

[53] Figures 6 and 7 represent the entire time sequence for the voltage and current collection on the line element for a given RF applied potential for frequencies that are 5 kHz above and below the proton plasma frequency. The blue curves represent the isothermal approximation (two moments) and the red curves represent the adiabatic approximation (three moments) with the term mAdB indicating milliamps on a decibel scale.

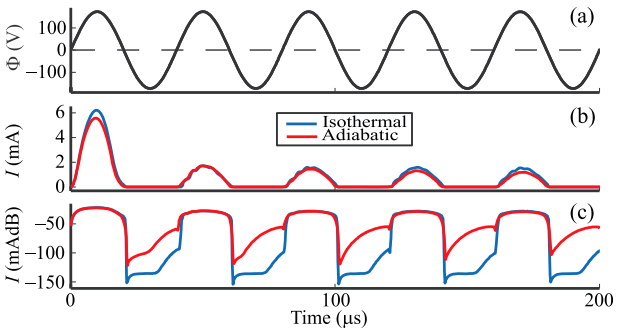

Figure 7. Current-voltage relationship for isotropic plasma with sinusoidal applied potential at 25 kHz. Blue, two moments; red, three moments. (a) Potential. (b) Current. (c) Current in dB.

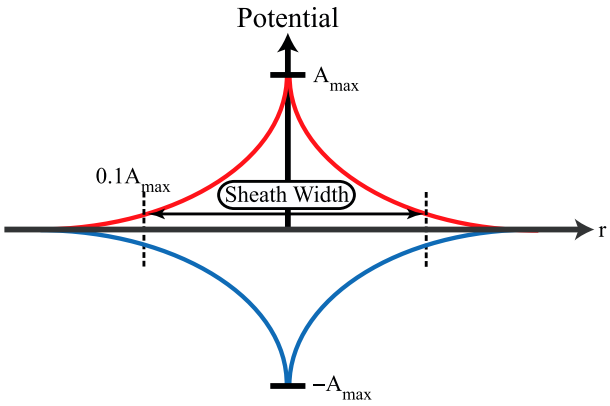

Figure 8. Diagram describing location of sheath edge.

[54] The sheath current I flowing onto the conductor is calculated by integrating the electric current density passing through the closed surface **S** defined by the exterior of the antenna element. This integral is represented by equation (5):

$$I = \oiint_{\mathbf{S}} \mathbf{J} \cdot d\mathbf{S} \tag{5}$$

where $J = \sum_{N} qn\mathbf{u}$ is the sum of the currents over all species N. For the 2-D line source represented in Figure 2, equation (5) amounts to a closed line integral in the $\hat{x}$-$\hat{y}$ plane representing a current per unit length.

[55] Figures 6 and 7 represent the current collection on the line element assuming an isotropic plasma. The current waveform is shown in both linear and log scales in order to illustrate the small contribution of the protons. Although the proton contribution to the current is negligible as seen per the rectified nature of the waveform, it is nevertheless nonzero. The other important point is that there is little difference between the isothermal and adiabatic approximations, suggesting that only a small number of moments are necessary in order to capture the relevant physics in sheath formation even under the collisionless assumption. This conclusion is supported by the earlier work of *Thiemann et al.* [1992] who compared both a two-moment fluid code and a particle in cell (PIC) code with good qualitative agreement in a collisionless isotropic plasma.

4.3. Three-Dimensional Dipole Antenna

[56] In this section we use our three-moment (adiabatic approximation) warm fluid code to examine the formation of the sheath surrounding a dipole antenna in a magnetized plasma in three dimensions. The electric dipole antenna considered is 20 m in length (tip-to-tip), 10 cm in diameter, and possesses a gap distance ranging from 20 cm to 2 m between the two antenna elements. For these simulations, we consider cases for which the operation of an electric dipole is under conditions corresponding to $L = 3$ in the geomagnetic equatorial plane. The antenna is excited using a sinusoidal interelement potential difference of ~86 V, approximately 500 times the background plasma potential which we denote as $500\Phi_p$. In addition, the same scaled proton-electron mass ratio of $(m_p/m_e) = 200$ is used as in the 2-D simulations. Only perpendicular antenna orientations with respect to the background magnetic field are considered as in the cold plasma simulation runs. Since there was virtually no difference in the behavior of the current collection for the 2-D cases for frequencies just above and below the proton plasma frequency, all 3-D simulation runs are performed at a frequency 5 kHz above the local proton plasma frequency, being 20 kHz at $L = 3$ respectively for the scaled mass ratio of $(m_p/m_e) = 200$. The lower hybrid resonance frequency at $L = 3$ is 761 Hz.

[57] As shown in section 4.1, a floating conductor immersed in a plasma develops a negative potential due to the high mobilities of the electrons. An electric dipole antenna experiences the same charging mechanism, if the collected charge is not removed from the antenna. However, unlike the floating wall, a transmitting antenna operating at high voltage relative to the background plasma potential accumulates a large number of electrons on the positively biased element during the sinusoidal cycle. This accumulation has the effect of producing a negative bias on the antenna elements that causes the entire system to drift to some negative DC potential. Instead of a symmetrically driven system, one of the elements is at a large negative potential while the other is at only a slight positive potential, forming asymmetric sheaths around the elements. In the following simulation runs, we examine a number of different scenarios by varying the plasma environment, gap spacing, and consider both a case for which an ideal charge removal system is used as well as that for which the electrons are allowed to accumulate.

[58] Since the actual location of the sheath 'edge' is quite arbitrary with no consensus on the defining criteria for this point [*Franklin*, 2004], in this paper we define the edge of the plasma sheath as a point in the field distribution at which the potential drops to within 10% of the maximum/minimum amplitude as shown in Figure 8.

[59] This definition of the sheath edge provides a much more stable result since the densities are constantly varying during the sinusoidal cycle with electrostatic waves propagating outward from the sheath region. The electrostatic potential distribution nevertheless remains periodic with the sheath edge remaining relatively unchanged throughout the simulation runs.

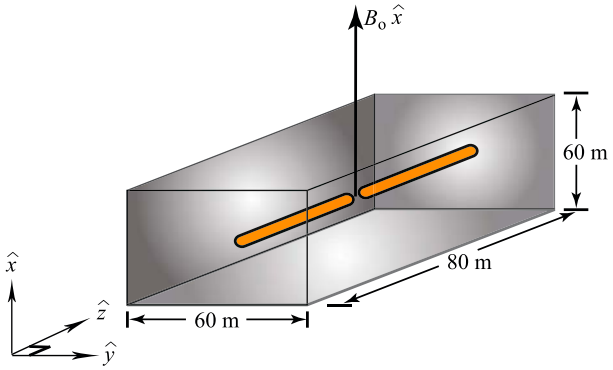

Figure 9. Three-dimensional computational domain at $L = 3$.

4.3.1. Antenna at $L = 3$ With Ideal Charge Removal System and 2 m Gap

[60] In this first case study, we consider the antenna to be located in the equatorial plane at $L = 3$ and assume that an ideal charge removal system extracts negative charge from the antenna. We initially start at $L = 3$ since the magnetic field is weaker and the Debye length is larger than the corresponding situation at $L = 2$. Thus, the $L = 3$ scenario is slightly more reminiscent of an isotropic plasma. A sketch of the simulation region is shown in Figure 9, with the $\hat{x}$-directed background magnetic field oriented perpendicular to the antenna.

[61] As with Figures 4 and 5 from the 2-D runs of the previous section, we present a time snapshot of the sheath during the peak of a sinusoidal cycle after a quasi-steady state has been reached. Figure 10 represents an orthographic projection of the sheath during the peak of the sinusoidal cycle after several periods in each slice plane.

[62] It can be seen from Figure 10 that the sheath is approximately 1 m wide and is virtually symmetric in each of the slice planes suggesting that the background magnetic field strength at $L = 3$ does not play much of a role in the steady state formation of the sheath. On the other hand, it is clearly seen from Figure 10 that the sheaths are not the same size on each element. This disparity is due to the fact that the expanding sheath does not instantaneously react to the applied voltage on the antenna, due to the mass difference and finite transit time of the protons and electrons through the sheath region. Therefore, the negative and positive sheaths surrounding each element fully expand to roughly the same size, but just not at the same time.

[63] Figure 11 represents the 1-D variation of the potential and number density for a radial slice taken through the midpoint of one of the dipole elements in the $\hat{x}$ direction, where the symbols t^+ and t^- in Figure 11 correspond to the first positive and negative peaks of the potential cycle after 5 periods of the sinusoidal waveform. All quantities shown by a dashed line correspond to t^+ and all solid lines correspond to quantities at t^-. Analogous to Figure 3, the steady state density variations for each species during the negative and positive peaks of the sinusoidal cycle are shown. The steady state situation represented in Figure 11 is reached after 5 periods of the waveform. Although the sheath itself is only 1 m wide as seen in Figures 10 and 11a, the presheath region, which is defined by the density pro-

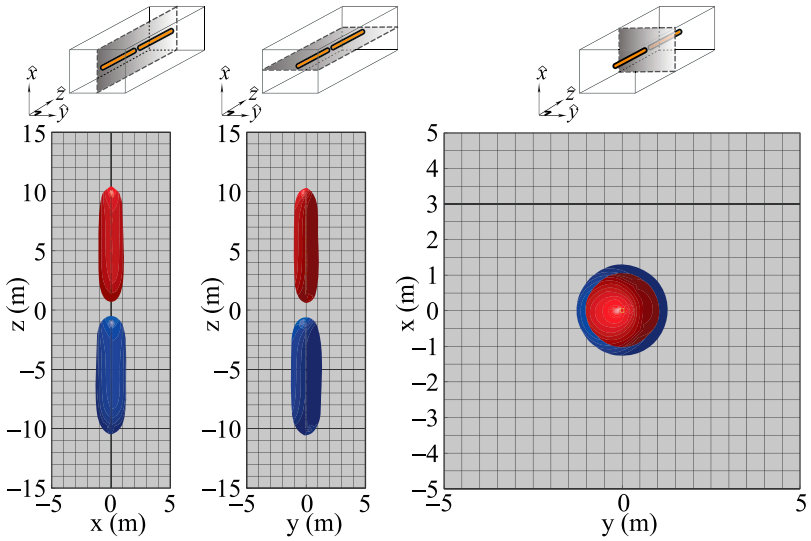

Figure 10. Orthographic projection of expanded sheath for $L = 3$ at maximum potential difference $500\Phi_p$. Operating frequency is at $f = 25$ kHz.

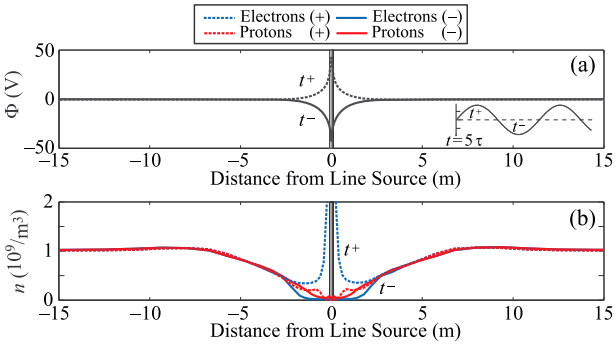

Figure 11. Electron and proton density variation for cross section through midpoint of dipole antenna element at $L = 3$. (a) Potential variation. (b) Electron and proton number densities.

files, extends several meters from the conductor. However, the large outward propagating density perturbation seen in the 2-D simulations has all but vanished by this time as can be seen in Figure 11b.

[64] The time domain waveforms in Figures 12a–12c represent the terminal characteristics for a single element of the dipole antenna located at $L = 3$, including potential, current and charge.

[65] The current on the element is calculated using equation (5) while the total charge Q on the element is calculated using equation (6):

$$Q = \oiint_{\mathbf{S}} \epsilon_0 \mathbf{E} \cdot d\mathbf{S} \tag{6}$$

where $\mathbf{E}$ is the electric field located at the surface of the dipole element. The charge is calculated by evaluating Gauss' law around the conductor where the electric field $\mathbf{E}$ is obtained from the solution of Poisson's equation via $\mathbf{E} = -\nabla\Phi$ where Φ is the potential applied to the element.

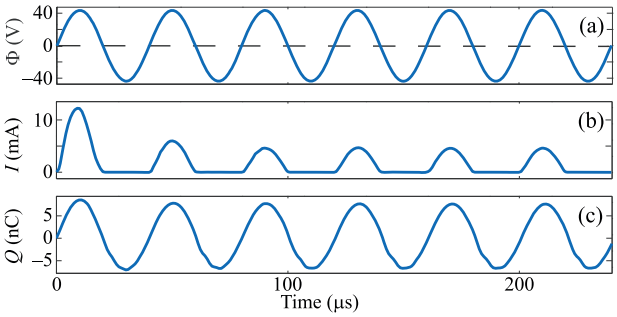

Figure 12. Terminal characteristics for 20 m antenna located at $L = 3$. (a) Voltage. (b) Current. (c) Charge.

[66] The presence of discontinuities in the current profile of Figure 12b produces high frequency content in the Fourier domain. As such, the resistance function, being highly nonlinear, would render the design of a tuning circuit a challenging task. It is seen from Figure 12 that the transient behavior during initial sheath formation has subsided after the first excitation period. Figure 12b exhibits the same rectified sine wave behavior present in the 2-D simulations resulting from negligible proton current flowing to the dipole element.

[67] In order to obtain a rough approximation of the steady state sheath's contribution to the terminal properties of the dipole antenna, we calculate the time domain root mean square (RMS) capacitance and resistance values using equations (7a) and (7b):

$$C_{\text{rms}} = \frac{Q_{\text{rms}}}{\Phi_{\text{rms}}} \tag{7a}$$

$$R_{\text{rms}} = \frac{\Phi_{\text{rms}}}{I_{\text{rms}}} \tag{7b}$$

where Φ_{rms}, I_{rms}, Q_{rms}, C_{rms} and R_{rms} are the RMS values of potential, current, charge, capacitance and resistance, respectively, of the sheath. Substituting the RMS values inferred from Figure 12 into the formulas given by equations (7a) and (7b), the time domain capacitance and resistance values at the driving frequency of 25 kHz are roughly $C \sim 169$ pF and $R \sim 13.7$ kΩ respectively.

[68] It is important to note that due to the nonlinear nature of the sheath, capacitance and resistance values used for tuning purposes are only valid for the peak sinusoidal voltage at which the transmitter is driven. Therefore, separate simulation runs would need to be made to calculate the sheath's contribution to the terminal impedance properties for each excitation waveform and driving potential used for a particular plasma environment. To complete the sheath analysis of the dipole antenna at $L = 3$, Figure 13 represents a plot of the time domain current flowing within the center of the gap between the elements.

[69] The current is determined by integrating the flux of particles flowing through a cross section with radius

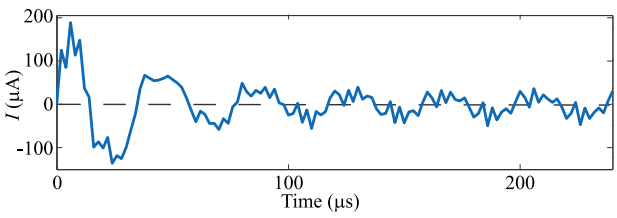

Figure 13. Interelement gap current for dipole antenna at $L = 3$.

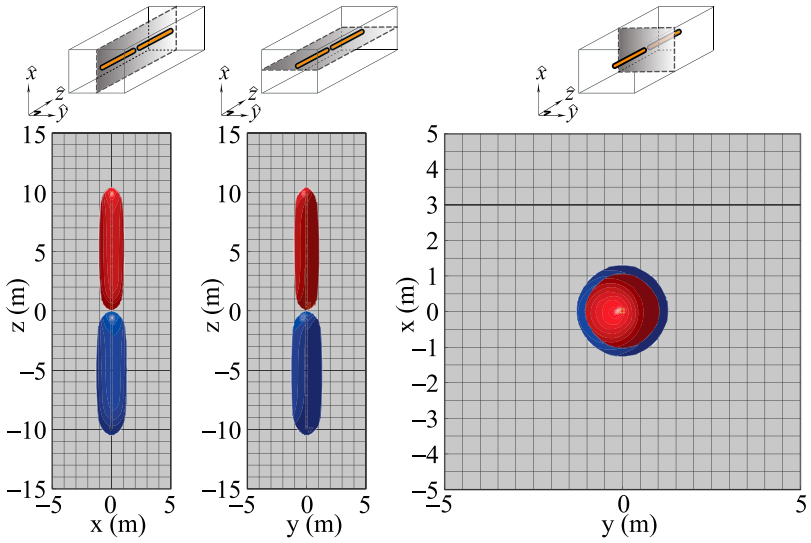

Figure 14. Orthographic projection of expanded sheath for L = 3 with 20 cm gap at maximum potential difference $500\Phi_p$. Operating frequency is at f = 25 kHz.

equal to the sheath width, being 1 m in this case. Results from this calculation allow us to determine the importance of interelement current flow on the total current moment of the antenna so as to ascertain whether or not the dipole elements should be spaced at some minimum distance to prevent adverse effects on the radiation resistance. From Figure 13, it is seen that after the initial transient has diminished (~60 μs), a steady state current is reached, having a peak value of approximately 40 μA. In the next few sections, we compare this value of the gap current with that of dipole antennas possessing a smaller gap spacing and without a charge removal system.

4.3.2. Antenna at L = 3 With Ideal Charge Removal System and 20 cm Gap

[70] For this next case study, we examine the sheath and terminal characteristics of a dipole antenna with an interelement gap that is 20 cm in width. As alluded to earlier, it is possible that with elements that are not as electrically isolated in the plasma as those with a larger gap spacing, substantial currents may flow from one dipole element to the other. Such a short circuit current could potentially cause a significant decrease in the radiation resistance of the antenna, with most of the radiation being produced by a current flowing across a very small area. This case study aims to assess the importance of this short-circuit effect.

[71] For this purpose, we assume an operating environment corresponding to L = 3 with a simulation space that is identical to that shown in Figure 9 with the only difference being the decrease in gap separation. Figure 14 represents the orthographic projection of the sheath for this case with results that are not markedly different from the case study at L = 3 with the 2 m gap separation.

[72] In fact, the sheaths surrounding the positive and negative elements are virtually identical to those for the larger gap spacing with the only difference being the separation distance. Likewise, the potential and number density variations for this case are not markedly different from Figure 11 and are therefore not shown.

[73] The RMS capacitance and resistance values determined from the terminal characteristics represented in Figure 15 are very similar to those found for the larger gap spacing, with values of $C \sim 187$ pF and $R \sim 13.5$ kΩ at the driving frequency. On the other hand, we might expect to see a significant difference between the two

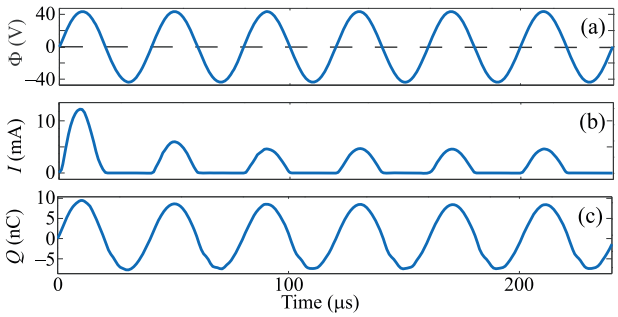

Figure 15. Terminal characteristics for 20 m antenna located at L = 3 with 20 cm gap. (a) Voltage. (b) Current. (c) Charge.

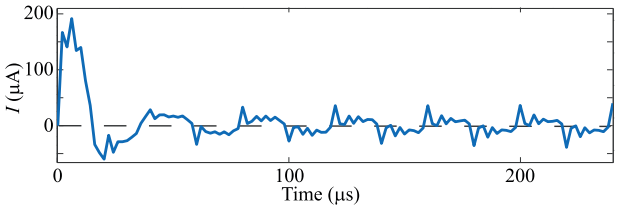

Figure 16. Interelement gap current for dipole antenna at $L = 3$ with 20 cm gap.

cases at $L = 3$ in the time domain gap current plot of Figure 16.

[74] Since our simulations are multidimensional, the geometry of the potential distribution within the computational space will change if the gap spacing is changed. This change in geometry will influence the particle trajectories. Furthermore, with a larger gap, it might be expected that the static magnetic field would have more influence on the particle trajectories. These changes might possibly affect the current flow in the gap between the two antenna elements.

[75] With the smaller gap separation, the electric field is much larger since the potential difference between the two antennas is over a distance that is a factor of 10 less for the case presented here. Surprisingly enough however, it can be seen from Figure 16 that the interelement gap current is roughly the same as that for antenna with the 2 m gap separation, still being ~40 μA. Although the velocity of the fluid element is undoubtedly larger due to the increase in electric field strength, this proportional increase in current is likely offset by the smaller density of particles present between the terminals of the antenna. This balance between density and field strength results in a current that is equivalent to that which is found in the case of antenna with a 2 m gap separation. We can conclude on this basis that a small interelement gap spacing does not have a detrimental effect on the current moment of the antenna versus that with a large gap separation.

4.3.3. Antenna at $L = 3$ Without Charge Removal System and 2 m Gap

[76] The final case study is that of a dipole antenna with no charge removal system present, allowing for charge buildup on the antenna surface. Analogous to the case of a floating conductor in a plasma, this net negative charge buildup due to the higher mobility of the electrons has the effect of producing a net negative potential bias on both elements of the antenna. This negative drift is readily seen in the orthographic projections of the sheath shown in Figure 17.

[77] As seen in Figure 17, the positive sheath is relatively small, being ~0.5 m in radius, while the negative sheath has a radius of ~1 m. The asymmetry between the positive and negative sheaths is most readily seen in Figure 18 representing the 1-D potential and density variation through one of the elements.

[78] The major difference between the floating dipole and that in which an ideal charge removal system is used is in the current collection due to the electron contribution on the element as shown in Figure 18b. Because the antenna system is allowed to drift to a large negative potential, it does not collect as many electrons during the positive potential cycle. However, because of the large

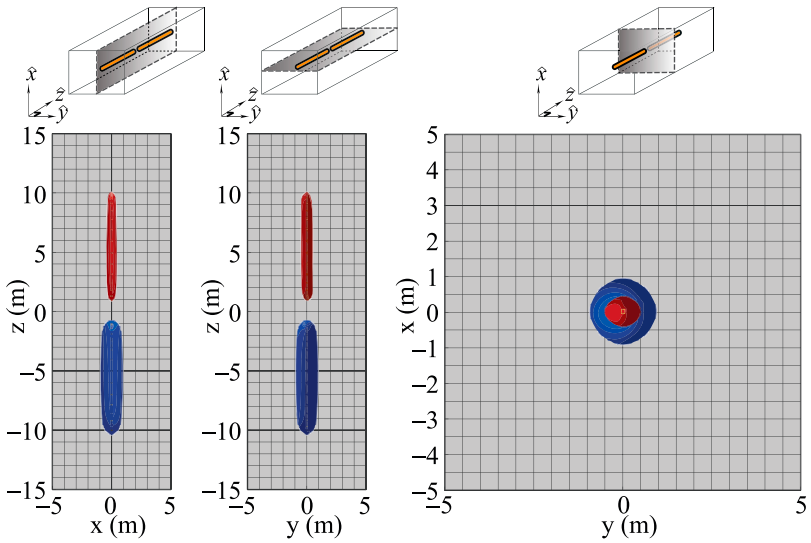

Figure 17. Orthographic projection of expanded sheath for $L = 3$ without ideal charge removal system at maximum potential difference $500\Phi_p$. Operating frequency is at $f = 25$ kHz.

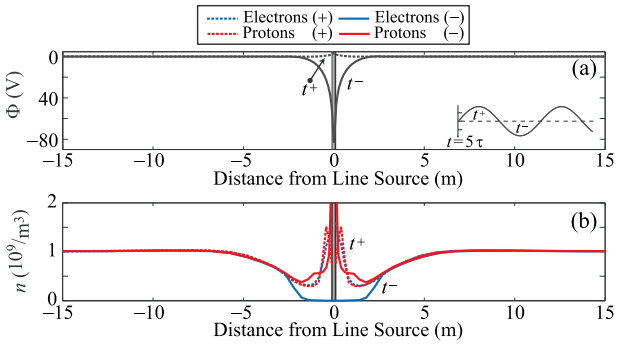

Figure 18. Electron and proton density variation for cross section through midpoint of dipole antenna element at $L = 3$ without ideal charge removal system. (a) Potential variation. (b) Electron and proton number densities.

negative bias, the number of protons collected on the antenna surface is much larger than that for the non-floating case, contributing to the small positive voltage seen in Figure 18a.

[79] The potential difference between the two elements is governed by the voltage source, although without the removal of excess charge, the entire system operates primarily in a negative voltage regime. Figure 19 shows the time domain terminal characteristics for both elements of the dipole antenna.

[80] As seen in Figure 19a, the potential on Element 1 stays just above 0 V during the first half cycle, while Element 2 drifts to a potential that is approximately twice the peak sinusoidal amplitude of the waveform. The voltage in Figure 19a is highly nonlinear, oscillating between the positive potential of only several volts, to a large negative potential, with the potential difference between the two elements equal to the 25 kHz driving sinusoid as shown in Figure 19b. The current waveforms for both elements, shown in Figure 19c, are vastly different than the case with an ideal charge removal system where it is seen that a large flux of protons is clearly hitting the antenna, unlike the previous case studies in which the current waveform resembled a rectified sinusoid. This large proton flux is also seen in Figure 18b where there is a significant proton density adjacent to the antenna during both negative and positive cycles, exceeding that of the electrons. In fact, the peak magnitude of the proton current over a single period, represented by $I < 0$ in Figure 19c, is roughly equal to half of the contribution due to the electrons, showing a significant increase over previous case studies.

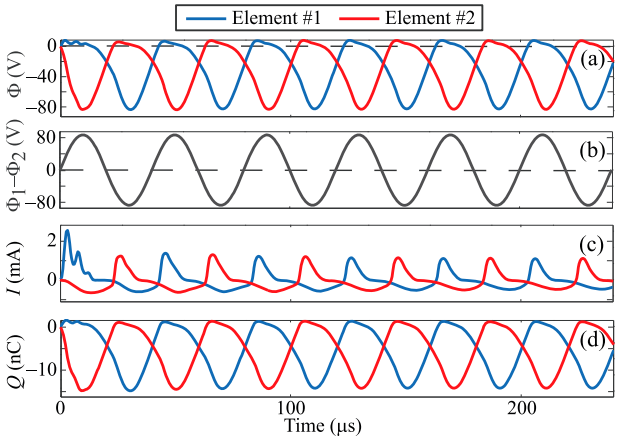

Figure 19. Terminal characteristics for 20 m antenna located at $L = 3$ without ideal charge removal system. (a) Voltage. (b) Interelement potential difference. (c) Current. (d) Charge.

[81] Although the RMS capacitance value is only slightly different from that of the previous case studies, the RMS resistance is significantly larger due to the reduced electron flux through the surface of the dipole element resulting from the negative potential bias of the system. The RMS capacitance and resistance values at the 25 kHz driving frequency for this floating dipole antenna are 177 pF and 107 kΩ respectively with the resistance value exhibiting a significant deviation from the previous calculations which utilized an ideal charge removal system.

[82] Finally in Figure 20, we examine the gap current for the floating dipole antenna. The gap current waveform is very similar to that of the other $L = 3$ case studies except that the magnitude is down by a factor of two being approximately 20 μA.

4.3.4. Proton Mass Scaling and Mobility

[83] The plasma frequencies at $L = 2$ and $L = 3$ are roughly 401 kHz and 284 kHz respectively. The excitation frequencies that are used in this paper range from 15 to 25 kHz which are far below the electron plasma frequency and lie in the vicinity for which whistler wave induced particle precipitation has been suggested by *Inan et al.* [2003] and *Song et al.* [2007].

[84] The important quantity concerning the actual mass of the protons is the corresponding plasma frequency of these particles which determines the rate at which these

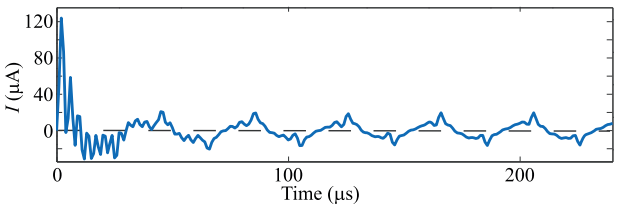

Figure 20. Interelement gap current for dipole antenna at $L = 3$ without ideal charge removal system.

particles can respond to a field resulting from a charge imbalance in the plasma. As long as the proton plasma frequency is much less than the electron plasma frequency (which is true if $m_i/m_e \geq 200$ as in our simulations), then underlying physics will be preserved as mentioned by *Calder and Laframboise* [1990]. We simulate sheath characteristics for frequencies above and below the ion plasma frequency which is 10 kHz for an unscaled proton mass at $L = 2$. Thus whether the ion mass is scaled or not (assuming that the $m_i \gg m_e$ criteria is satisfied) the same behavior will be seen in the current collection and charge accumulation on the antenna resulting from ion motion as discussed by *Calder and Laframboise* [1990] and related works for DC applied potentials on spherical electrodes. And in a self-consistent way, we show that this motion has a significant effect on the characteristics of the sheath. In the Bohm floating sheath analysis, it is the motion of the ions that shields further electrons from being collected on the conducting surface. Thus in order to develop any sheath, ions must be mobile. Thus, the immobile ion assumption made in past work is not accurate in sheath development for the cases considered here.

4.3.5. Antenna Tuning

[85] In all of the cases considered, the nonlinear structure of the sheath is readily apparent in terms of the terminal characteristics and hence, tuning properties. For the sinusoidal waveforms considered, the structure of the sheath does exhibit a steady state nature with each of the dipole elements possessing very similar characteristics in terms of voltage, charge and current draw. Thus one might expect, based on our findings, that the tuning circuit used to maximize the power delivered to the antenna would be the same for each dipole element, albeit complicated. It is also clear from our warm plasma findings that for frequencies above f_{LHR}, the complex impedance of the antenna is dominated by the sheath characteristics as opposed to the almost perfectly tuned antenna that the cold plasma model predicts [*Bell et al.*, 2006].

[86] The physics of sheath formation is inherently a nonlinear problem. Therefore given a sinusoidal input, one would not expect a sinusoidal steady state output. Indeed, for the final case study presented in the results section, a sinusoidal input produces a highly nonlinear, though periodic current waveform on the elements of the dipole. In many of the references listed in the introduction of our manuscript concerning collisionless plasma sheath formation [*Calder and Laframboise*, 1990; *Thiemann et al.*, 1992] for instance, the presence of instabilities was noted along with other nonlinear effects for DC applied potentials with the sinusoidal variation of our paper being a more complicated case study. These nonlinear effects noticed in the above mentioned DC analysis may or may not last for long periods of time which suggests that the sheath in a collisionless plasma may exhibit anything but a steady state structure. Most previous work involving antennas operating in a space plasma utilize some form of linearized plasma environment for which sinusoidal steady state behavior is an implicit assumption. Therefore, all nonlinear effects are suppressed and would not be observed. In addition, most of the antenna papers listed in section 1 use a cold plasma analysis which does not self-consistently support the formation of the plasma sheath since by design, a cold plasma analysis only allows for small perturbations of plasma parameters (i.e., density, velocity) about the ambient value. Our warm plasma model is not restricted by these assumptions.

[87] The results presented in our warm plasma model constitute one of the first complete attempts to determine the plasma sheath contribution to the near-field antenna-plasma coupling response. This coupling would need to separately be determined for every driving potential and frequency content of the source excitation waveform considered as well as for each environment in which the antenna will be operating. Though the capacitance and resistance values calculated in this section are not meant to be used in practical design implementation, they do provide a first order approximation of the sheath's impact on tuning requirements. The generality of our simulation tool allows for its use in determining the near field coupling of antennas of arbitrary geometry and operating environments making it a flexible and useful tool in future antenna design and analysis.

5. Summary

[88] In this paper, we have addressed the near-field coupling of electric dipole antennas to a collisionless magnetized plasma using a multimoment fluid approach. The warm plasma fluid equations, provided the capability to examine both transient and steady state electrostatic sheath formation from which we were able to draw a number of conclusions based on these results. The first result is that the nonlinear sheath dynamics possess periodicity with respect to sinusoidal waveform excitation, exhibiting a quasi-steady state structure. The current, and voltage waveforms of the three dimensional antenna exemplify the nonlinear nature of the plasma sheath by exhibiting large deviations from sinusoidal behavior for a given sinusoidal input. Antenna charging is quantified in the absence of a charge removal system. This has the effect of greatly reducing the sheath radius around the positive dipole element and placing the system in a negatively biased operating region due to the more mobile electrons. In addition, we have shown that the Boltzmann factor is not adequate in describing the density modification to the distribution function under AC applied potentials in a collisionless plasma.

It has been shown that a decrease in gap spacing will not adversely affect the current moment of a transmitting antenna. We find that the common assumption of immobile ions used in past work is not adequate when considering thermal effects under the influence of driving frequencies in the vicinity of the ion plasma frequency. It has been shown that the density of protons varies significantly throughout the sheath region and contributes to the current collection. And finally, the fact that a comparison between the two- and three-moment truncation schemes yields different results suggests that capturing more of the moments in the hydrodynamic approach allows for more flexibility and therefore more accuracy in describing the evolution of the distribution function absent in a cold plasma formulation.

[89] **Acknowledgments.** This research was supported by AFOSR grant F49620-03-1-0338, by MURI grant 1109406, and by Sequoia Technologies grant 1109381.

References

Abel, B., and R. Thorne (1998), Electron scattering loss in Earth's inner magnetosphere: 1. Dominant physical processes, *J. Geophys. Res.*, *103*(A2), 2385–2396.

Albert, J. (2001), Comparison of pitch angle diffusion by turbulent and monochromatic whistler waves, *J. Geophys. Res.*, *106*(A5), 8477–8482.

Baker, D., H. Weil, and L. Bearce (1973), Impedance and large signal excitation of satellite-borne antennas in the ionosphere, *IEEE Trans. Antennas Propag.*, *21*(5), 672–679.

Balay, S., K. Buschelman, V. Eijkhout, W. Gropp, D. Kaushik, M. Knepley, L. McInnes, B. Smith, and H. Zhang (2004), *PETSc Users Manual*, Argonne Natl. Lab., Argonne, Ill.

Bell, T., U. Inan, M. Platino, J. Pickett, P. Kossey, and E. Kennedy (2004), CLUSTER observations of lower hybrid waves excited at high altitudes by electromagnetic whistler mode signals from the HAARP facility, *Geophys. Res. Lett.*, *31*, L06811, doi:10.1029/2003GL018855.

Bell, T., U. Inan, and T. Chevalier (2006), Current distribution of a VLF electric dipole antenna in the plasmasphere, *Radio Sci.*, *41*, RS2009, doi:10.1029/2005RS003260.

Bezrukikh, V. V., G. A. Kotova, L. A. Lezhen, J. Lemaire, V. Pierrard, and Y. I. Venediktov (2003), Dynamics of temperature and density of cold protons of the Earth's plasmasphere measured by the auroral probe/alpha-3 experiment data during geomagnetic disturbances, *Cosmic Res.*, *41*(4), 392–402.

Bittencourt, J. (2003), *Fundamentals of Plasma Physics*, 3rd ed., Springer, New York.

Bohm, D. (1949), *The Characteristics of Electrical Discharges in Magnetic Fields*, edited by A. Guthrie and R. K. Wakerling, chap. 3, p. 77, McGraw-Hill, New York.

Borovsky, J. (1988), The dynamic sheath: Objects coupling to plasmas on electron-plasma-frequency time scales, *Phys. Fluids*, *31*(5), 1074–1100.

Calder, A. C., and J. G. Laframboise (1990), Time-dependent sheath response to abrupt electrode voltage changes, *Phys. Fluids B*, *2*(3), 655–666.

Calder, A. C., G. W. Hulbert, and J. G. Laframboise (1993), Sheath dynamics of electrodes stepped to large negative potentials, *Phys. Fluids B*, *5*(3), 674–690.

Carpenter, D., and R. Anderson (1992), An ISEE/Whistler model of equatorial electron density in the magnetosphere, *J. Geophys. Res.*, *97*(A2), 1097–1108.

Carpenter, D., T. Bell, U. Inan, R. Benson, V. Sonwalkar, B. Reinisch, and D. Gallagher (2003), Z-mode sounding within propagation cavities and other inner magnetospheric regions by the RPI instrument on the IMAGE satellite, *J. Geophys. Res.*, *108*(A12), 1421, doi:10.1029/2003JA010025.

Chust, T., and G. Belmont (2006), Closure of fluid equations in collisionless magnetoplasmas, *Phys. Plasmas*, *13*(1), 012506.

Franklin, R., and W. Han (1988), The stability of the plasma-sheath with secondary emission, *Plasma Phys. Controlled Fusion*, *30*(6), 771–784.

Franklin, R. N. (2004), Where is the sheath edge?, *J. Phys. D Appl. Phys.*, *37*(9), 1342–1345.

Hockney, R. W., and J. W. Eastwood (1981), *Computer Simulation Using Particles*, McGraw-Hill, New York.

Inan, U., T. Bell, J. Bortnik, and J. Albert (2003), Controlled precipitation of radiation belt electrons, *J. Geophys. Res.*, *108*(A5), 1186, doi:10.1029/2002JA009580.

Kurganov, A., and E. Tadmor (2000), New high-resolution central schemes for nonlinear conservation laws and convection-diffusion equations, *J. Comput. Phys.*, *160*(1), 241–282.

Labrunie, S., J. A. Carrillo, and P. Bertrand (2004), Numerical study on hydrodynamic and quasineutral approximations for collisionless two-species plasmas, *J. Comput. Phys.*, *200*(1), 267–298.

Laframboise, J. G. (1997), Current collection by a positively charged spacecraft: Effects of its magnetic presheath, *J. Geophys. Res.*, *102*(A2), 2417–2432.

Langmuir, I. (1929), The interaction of electron and positive ion space charges in cathode sheaths, *Phys. Rev.*, *33*(6), 0954–0989.

Ma, T., and R. Schunk (1989), A fluid model of high voltage spheres in an unmagnetized plasma, *Plasma Phys. Controlled Fusion*, *31*(3), 399–421.

Ma, T., and R. Schunk (1992a), High negative voltage spheres in an unmagnetized plasma: Fluid simulation, *Plasma Phys. Controlled Fusion*, *34*(5), 783–799.

Ma, T., and R. Schunk (1992b), High-voltage spheres in an unmagnetized plasma: Long-term evolution and rise-time effects, *Plasma Phys. Controlled Fusion*, *34*(5), 767–781.

Mlodnosky, R. F., and O. K. Garriott (1963), The V. L. F. admittance of a dipole in the lower ionosphere, in *Proceedings of the International Conference on the Ionosphere, London, July 1962*, p. 484, Inst. of Phys. and Phys. Soc., London.

Palmadesso, P. (1989), Interaction of a spherical high voltage probe with the space environment: Electron trapping, current drain and collective process, in *Proceedings of the Intersociety Energy Conversion Engineering Conference*, vol. 1, pp. 435–440, IEEE Press, Piscataway, N. J.

Parker, L., and B. Murphy (1967), Potential buildup on electron-emitting ionospheric satellite, *J. Geophys. Res.*, *72*(5), 1631–1636.

Parker, S. E., A. Friedman, S. L. Ray, and C. K. Birdsall (1993a), Bounded multiscale plasma simulation—Application to sheath problems, *J. Comput. Phys.*, *107*(2), 388–402.

Parker, S. E., R. J. Procassini, C. K. Birdsall, and B. I. Cohen (1993b), A suitable boundary condition for bounded plasma simulation without sheath resolution, *J. Comput. Phys.*, *104*(1), 41–49.

Platino, M., U. Inan, T. Bell, D. Gurnett, J. Pickett, P. Canu, and P. Decreau (2005), Whistlers observed by the cluster spacecraft outside the plasmasphere, *J. Geophys. Res.*, *110*, A03212, doi:10.1029/2004JA010730.

Shkarofsky, I. (1972), Nonlinear sheath admittance, currents, and charges associated with high peak voltage drive on a VLF/ELF dipole antenna moving in the ionosphere, *Radio Sci.*, *7*(4), 503–523.

Song, P., B. W. Reinisch, V. Paznukhov, G. Sales, D. Cooke, J. N. Tu, X. Huang, K. Bibl, and I. Galkin (2007), High-voltage antenna-plasma interaction in whistler wave transmission: Plasma sheath effects, *J. Geophys. Res.*, *112*, A03205, doi:10.1029/2006JA011683.

Spiteri, R. J., and S. J. Ruuth (2002), A new class of optimal high-order strong-stability-preserving time discretization methods, *SIAM J. Numer. Anal.*, *40*(2), 469–491.

Thiemann, H., T. Z. Ma, and R. W. Schunk (1992), High voltage spheres in an unmagnetized plasma: Fluid and PIC simulations, *Adv. Space Res.*, *12*(12), 57–60.

Wang, S. B., and A. E. Wendt (1999), Sheath thickness evaluation for collisionless or weakly collisional bounded plasmas, *IEEE Trans. Plasma Sci.*, *27*(5), 1358–1365.

T. F. Bell, T. W. Chevalier, and U. S. Inan, Department of Electrical Engineering, Stanford University, 351 Packard EE Bldg., Stanford, CA 94305, USA. (timothyc@stanford.edu)